Integrated photoelasticity measurements of a three-dimensional laminar flow: second-order stress terms in the stress-optic law

Kento NAKAMINE[1], Yuto YOKOYAMA[1], William Kai Alexander WORBY[1], Masakazu MUTO[2,*] and Yoshiyuki TAGAWA[1,*]

[1] *Department of Mechanical Systems Engineering, Tokyo University of Agriculture and Technology*
[2] *Department of Mechanical Engineering, Nagoya Institute of Technology*
[*] *muto.masakazu@nitech.ac.jp, tagawayo@cc.tuat.ac.jp*

Abstract: This study experimentally validates a stress-optic law for a three-dimensional flow using integrated photoelasticity. In this stress-optic law, the stress is related to the two photoelastic parameters — the phase retardation Δ and orientation ϕ — of elliptically-polarized light. Previous studies have examined the stress-optic law of three-dimensional flows, but the importance of the second-order stress terms in the three-dimensional stress-optic law, i.e., those relating to the stress component along the camera's optical axis, have not yet been experimentally validated. In this work, we measure the retardation of a steady laminar flow of a Newtonian fluid (cellulose nanocrystal suspension of 0.5 wt%) in a square channel and compare it with the theoretical prediction. Remarkably, the theoretical result including the second-order stress terms shows good agreement with the experimental result for various flow rates, while the calculation without these terms, which is often referred to as a "stress-optic law", results in a significant deviation from the measurements. Therefore, proper consideration of the second-order stress terms in the three-dimensional stress-optic law is crucial for integrated photoelasticity measurements of three-dimensional flow fields.

1. Introduction

In recent years, there has been a high demand for non-contact optical measurements of three-dimensional stress fields in fluids. Photoelasticity has great potential as a method of measuring such fields [1, 2]. It is a solid-state stress-measurement technique that has been extensively studied over the last 50 years, utilizing the retardation of polarized light [3, 4]. When circularly-polarized light is incident on a photoelastic material under stress loading, birefringence occurs depending on the stress state, and elliptically-polarized light with retardation Δ and orientation ϕ is emitted. Δ and ϕ are related to the principal stress difference and the principal stress direction, respectively [5].

In photoelasticity, the stress can be estimated from Δ using the stress-optic law [6–8]. When the stress field is uniform along the camera's optical axis, the retardation and the stress can be related by the two-dimensional stress-optic law, i.e., the secondary principal stress difference [9–11]. Note that the secondary principal stress difference is the principal stress difference projected onto the plane perpendicular to the camera's optical axis. In the case of a three-dimensional stress field measurement, i.e., when the stress field is not uniform along the camera's optical axis, one should take into account the three-dimensional stress-optic law and the integrated photoelasticity [1, 2, 9, 12]. The integrated photoelasticity requires the use of Mueller calculus (calculations using the Stokes parameter and the Mueller matrix) as well as the stress-optic law [13, 14], as described later in Section 2.1.

In recent years, there have been some reports on the application of photoelasticity to quasitwo-dimensional fluid flows [15–19]. In particular, several measurements have used an aqueous cellulose nanocrystal suspension (hereinafter, CNC suspension) as the photoelastic fluid [15, 20–22] to show that the above two-dimensional measurement principle can be successfully applied [23, 24]. These studies have shown the great potential of photoelasticity for flow field measurements.

McAfee and Pih [25] observed three-dimensional flow in a channel and stated that "the isoclinic (retardation in this paper) was dependent on shear strain rates both normal and parallel (camera's optical axis in this paper) to the light ray", but they did not show the direct relation between the stress-optic law and their observation. Doyle et al. [14] derived the extended stress-optic law for measuring a three-dimensional flow by considering the stress acting on the plane parallel to the camera's optical axis. They also highlighted the importance of the stress component along the camera's optical axis, i.e., second-order stress terms in the extended stress-optic law, although they did not validate their theory with experiments. Aben and Puro [13] discussed photoelastic measurements of a three-dimensional fluid flow by referring to Doyle's work. They used the three-dimensional stress-optic law but neglected the second-order terms. Other significant works [16, 26, 27] have also neglected these second-order terms. However, the results of some studies have indicated that there is a discrepancy between theory and experiment, especially at the channel center [16, 27]. To the best of the author's knowledge, the three-dimensional stress-optic law has never been directly validated with photoelastic measurements of a three-dimensional flow.

Therefore, the purpose of this study is to experimentally validate the extended stress-optic law for three-dimensional flows using integrated photoelasticity. A steady laminar flow of a Newtonian fluid in a square channel is chosen as the focus of this work because an analytical solution for the stress field is available for this case.

This paper is organized as follows. Section 2.1 describes integrated photoelasticity. In Section 2.2, we revisit the relation between the strain rate and dielectric constant in electromagnetism and the stress-optic law. According to the stress-optic law, the optical parameters (the retardation Δ and orientation ϕ) can be expressed as a combination of the first-order and second-order stress terms. As noted above, only the first-order stress term in the stress-optic law has been considered in recent works. Section 2.3 explains the experimental method and Section 2.4 describes the theoretical retardation field of a Newtonian laminar flow in a square channel. Section 3 describes the experimental observations and provides a comparison and discussion of the experimental and theoretical values. In Section 4, it is concluded that the second-order stress term in the three-dimensional stress-optic law should be properly considered in stress measurements of three-dimensional flows.

2. Method

In this section, we first explain integrated photoelasticity in the context of our measurement system and describe the stress-optic law. We then explain how the experimental retardation is measured and how the theoretical retardation is calculated.

2.1. Integrated photoelasticity with an optically equivalent model

This section explains integrated photoelasticity with an optically equivalent model in the context of our experimental system.

A material with a three-dimensional stress field can be reduced to an optically equivalent model consisting of one linear retarder and one rotator [28–30]. In general, the retardation Δ due to the linear retarder, the orientation ϕ_1 of the linear retarder, and the rotation ϕ_2 due to the rotator must be considered. The reason for considering ϕ_2 is that the direction of the secondary principal stress is generally rotated around the camera's optical axis in a three-dimensional stress field. On the contrary, if the direction of the secondary principal stress does not rotate around the camera's optical axis, as in a two-dimensional stress field, only the retardation Δ due to the linear retarder and the direction of the linear retarder ϕ_1 need to be considered. In other words, when a three-dimensional stress field is divided into sufficiently thin plates that can be assumed to be two-dimensional stress fields, each plate can be considered to consist of a linear retarder without a rotator, i.e., $\phi_2 = 0$. In this case, the polarization state of light passing through the three-dimensional stress field can be calculated by multiplying the Mueller matrices of each optically equivalent model [11, 31].

Figure 1 shows a schematic diagram of the measurement principle used in this study. The camera's optical axis is the z-axis. Unpolarized light emitted from a monochromatic light source passes through both a linear polarizer and a quarter-wave plate and becomes circularly-polarized light. The circularly-polarized light then passes through a three-dimensional laminar flow in a square channel and becomes elliptically-polarized light. The elliptically-polarized light is characterized by two optical parameters — the retardation Δ [nm] and the orientation ϕ [deg]. Both Δ and ϕ are measured using the phase-shifting method [32–35]. To examine the relationship between the optical parameters (Δ and ϕ) and the three-dimensional stress field in a flow, the concept of integrated photoelasticity with an optically equivalent model [28, 31, 36] is adopted. In the optically equivalent model, a three-dimensional stress field is virtually divided into N infinitesimal thin plates that can be assumed to be like two-dimensional stress fields [31]. Each plate can be replaced by an optically equivalent model that is characterized by $\Delta^{(i)}$ and $\phi^{(i)}$ [30, 37].

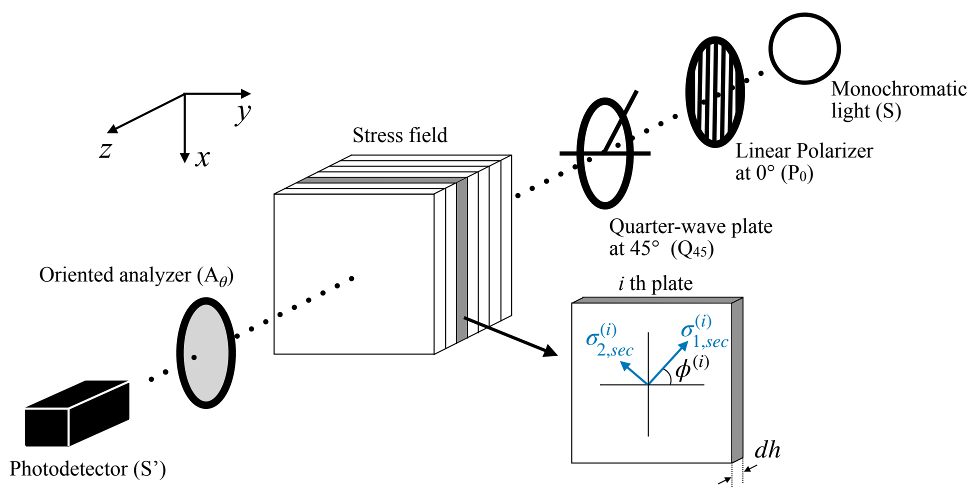

Fig. 1. A schematic diagram of the measurement principle. Circularly-polarized light is transmitted through the stress field. The light modulated by the stress field is measured using a polarization camera that consists of an oriented analyzer and photodetector. The stress field can be divided into N infinitesimal thin plates that can be assumed to be two-dimensional stress fields that can be replaced by an optically equivalent model. The integrated retardation Δ and orientation ϕ are calculated using Mueller calculus with the Stokes parameter and the Mueller matrix.

The retardation Δ of outgoing polarized light passing through all N thin plates in the three-dimensional stress field can be calculated using Mueller calculus with the Stokes parameters and Mueller matrix [12, 31]. The Stokes vectors $\mathbf{S}$ and $\mathbf{S_{object}}$, which characterize the respective polarized states of the incident unpolarized light and the outgoing polarized light modulated by the stress field [38], are expressed as follows:

$$\mathbf{S} = \begin{bmatrix} S_0 \\ S_1 \\ S_2 \\ S_3 \end{bmatrix} = \begin{bmatrix} I \\ 0 \\ 0 \\ 0 \end{bmatrix}, \tag{1}$$

$$\mathbf{S}_{\text{object}} = \begin{bmatrix} S_{\text{object},0} \\ S_{\text{object},1} \\ S_{\text{object},2} \\ S_{\text{object},3} \end{bmatrix}, \tag{2}$$

where I is the intensity of the incident light emitted from the light source. $\mathbf{S}_{\text{object}}$ is obtained by multiplying $\mathbf{S}$ by the Mueller matrices of each optical element and the optically equivalent model of each thin plate as follows:

$$\mathbf{S_{object}} = \mathbf{X^{(N)}} \ldots \mathbf{X^{(i)}} \ldots \mathbf{X^{(2)}} \mathbf{X^{(1)}} \mathbf{Q_{45}} \mathbf{P_0} \mathbf{S}, \tag{3}$$

where $\mathbf{X}^{(i)}$ is the Mueller matrix of the i-th thin plate,

$$\mathbf{X^{(i)}} = \begin{bmatrix} 1 & 0 & 0 & 0 \\ 0 & 1-(1-\cos\Delta^{(i)})\sin^2 2\phi^{(i)} & (1-\cos\Delta^{(i)})\sin 2\phi^{(i)}\cos 2\phi^{(i)} & -\sin\Delta^{(i)}\sin 2\phi^{(i)} \\ 0 & (1-\cos\Delta^{(i)})\sin 2\phi^{(i)}\cos 2\phi^{(i)} & 1-(1-\cos\Delta^{(i)})\cos^2 2\phi^{(i)} & \sin\Delta^{(i)}\cos 2\phi^{(i)} \\ 0 & \sin\Delta^{(i)}\sin 2\phi^{(i)} & -\sin\Delta^{(i)}\cos 2\phi^{(i)} & \cos\Delta^{(i)} \end{bmatrix}, \tag{4}$$

and $\Delta^{(i)}$ and $\phi^{(i)}$ can be obtained using the stress-optic law, as described in Section 2.2. $\mathbf{P}_0$ and $\mathbf{Q}_{45}$ are the Mueller matrices of the linear polarizer set to 0° and the quarter-wave plate at 45°, respectively,

$$\mathbf{P_0} = \frac{1}{2}\begin{bmatrix} 1 & 1 & 0 & 0 \\ 1 & 1 & 0 & 0 \\ 0 & 0 & 0 & 0 \\ 0 & 0 & 0 & 0 \end{bmatrix}, \tag{5}$$

$$\mathbf{Q_{45}} = \begin{bmatrix} 1 & 0 & 0 & 0 \\ 0 & 0 & 0 & -1 \\ 0 & 0 & 1 & 0 \\ 0 & 1 & 0 & 0 \end{bmatrix}. \tag{6}$$

The retardation Δ of the outgoing light from the stress field can be measured using a four-step phase-shifting method [33, 34, 39]. The Stokes vectors $\mathbf{S}_\theta$ of polarized light passing through a linear polarizer rotated by orientation θ can be described as

$$\mathbf{S}_\theta = \begin{bmatrix} S_{\theta,0} \\ S_{\theta,1} \\ S_{\theta,2} \\ S_{\theta,3} \end{bmatrix} = \mathbf{A}_\theta \mathbf{S}_{\mathbf{object}}, \tag{7}$$

where $\mathbf{A}_\theta$ is the Mueller matrix of the analyzer,

$$\mathbf{A}_\theta = \frac{1}{2} \begin{bmatrix} 1 & \cos 2\theta & \sin 2\theta & 0 \\ \cos 2\theta & \cos^2 2\theta & \sin 2\theta \cos 2\theta & 0 \\ \sin 2\theta & \sin 2\theta \cos 2\theta & \sin^2 2\theta & 0 \\ 0 & 0 & 0 & 0 \end{bmatrix}. \tag{8}$$

The first component of the Stokes vector, $S_{\theta,0}$, can be measured as the light intensity I_θ. The calculation of Eqs. (1)–(8) gives the relationship between the light intensity I_θ and the optical parameters of the outgoing polarized light, Δ and ϕ, as

$$I_\theta = \frac{1}{4} I(1 - \sin\Delta \sin 2\phi \cos 2\theta + \sin\Delta \cos 2\phi \sin 2\theta). \tag{9}$$

Using the four-step phase-shifting method with $\theta = 0°, 45°, 90°$, and $135°$, the relationship between the light intensities of each angle θ and the optical parameters, Δ and ϕ, can be described as

$$\begin{aligned} I_{0°} &= \frac{1}{4} I(1 - \sin\Delta \sin 2\phi), && (10) \\ I_{45°} &= \frac{1}{4} I(1 + \sin\Delta \cos 2\phi), && (11) \\ I_{90°} &= \frac{1}{4} I(1 + \sin\Delta \sin 2\phi), && (12) \\ I_{135°} &= \frac{1}{4} I(1 - \sin\Delta \cos 2\phi), && (13) \\ I &= I_{0°} + I_{45°} + I_{90°} + I_{135°}. && (14) \end{aligned}$$

Finally, the retardation Δ of the polarized light passing through the stress field is calculated as

$$\Delta = \frac{\lambda}{2\pi} \sin^{-1} \frac{\sqrt{(I_{90°} - I_{0°})^2 + (I_{45°} - I_{135°})^2}}{I/2}, \tag{15}$$

where λ is the wavelength of the light source.

2.2. *Stress-optic law*

In this section, we describe the stress-optic law used to calculate $\Delta^{(i)}$ and $\phi^{(i)}$ in Eq. (4).

Birefringence is caused by the phase retardation of light due to the anisotropic refractive index tensor of a photoelastic material when loaded by stress. The refractive index of the material is determined by the relative permittivity, which is also known as the dielectric constant. The parameters Δ and ϕ are related to the components of the dielectric tensor in the x-y plane $(\varepsilon_{xx}, \varepsilon_{yy}, \varepsilon_{xy})$ as follows [13, 14]:

$$\Delta \cos 2\phi = \frac{1}{2n_0}\left(\varepsilon_{xx} - \varepsilon_{yy}\right) dh, \tag{16}$$

$$\Delta \sin 2\phi = \frac{1}{n_0}\varepsilon_{xy} dh,, \tag{17}$$

where n_0 is the initial refractive index of the material and dh is the thickness of a thin plate. The optical effect is a function of the strain rate $\dot{e}_{jk}$ [13, 14]:

$$\frac{1}{2n_0}\varepsilon_{jk} = f(\dot{e}_{jk}) \tag{18}$$

By using the Cayley–Hamilton theorem [13, 14], the optical effect can be written as

$$\frac{1}{2n_0}\varepsilon_{jk} = \alpha_0\delta_{jk} + \alpha_1\dot{e}_{jk} + \alpha_2\dot{e}_{jl}\dot{e}_{lk}, \tag{19}$$

where α_0, α_1, and α_2 are the material-specific constants and δ_{jk} is the Kronecker delta. Here, j, k, and l are Einstein notation indices. Therefore, as described in previous studies [13, 14], the relationship between the optical parameters of the i-th plate $(1 \leq i \leq N)$ and the components of the strain rate tensor can be expressed by the following equations using Eqs. (16) and (17):

$$\Delta^{(i)} \cos 2\phi^{(i)} = \left\{\alpha_1\left(\dot{e}_{xx}^{(i)} - \dot{e}_{yy}^{(i)}\right) + \alpha_2\left[\left(\dot{e}_{xx}^{(i)} + \dot{e}_{yy}^{(i)}\right)\left(\dot{e}_{xx}^{(i)} - \dot{e}_{yy}^{(i)}\right) + \left(\dot{e}_{yz}^{(i)}\right)^2 - \left(\dot{e}_{xz}^{(i)}\right)^2\right]\right\} dh \tag{20}$$

$$\Delta^{(i)} \sin 2\phi^{(i)} = \left\{2\alpha_1\dot{e}_{xy}^{(i)} + \alpha_2\left[2\left(\dot{e}_{xx}^{(i)} + \dot{e}_{yy}^{(i)}\right)\dot{e}_{xy}^{(i)} + 2\dot{e}_{yz}^{(i)}\dot{e}_{xz}^{(i)}\right]\right\} dh \tag{21}$$

For a Newtonian fluid, the shear stress is proportional to the strain rate, i.e., $\sigma_{jk}^{(i)} = \mu\dot{e}_{jk}^{(i)}$, where μ is the liquid viscosity. Thus, $\Delta^{(i)}$ and $\phi^{(i)}$ can be expressed using stress instead of the strain rate, as in the following equations.

$$\Delta^{(i)} \cos 2\phi^{(i)} = \left\{C_1\left(\sigma_{xx}^{(i)} - \sigma_{yy}^{(i)}\right) + C_2\left[\left(\sigma_{xx}^{(i)} + \sigma_{yy}^{(i)}\right)\left(\sigma_{xx}^{(i)} - \sigma_{yy}^{(i)}\right) + \left(\sigma_{yz}^{(i)}\right)^2 - \left(\sigma_{xz}^{(i)}\right)^2\right]\right\} dh, \tag{22}$$

$$\Delta^{(i)} \sin 2\phi^{(i)} = \left\{2C_1\sigma_{xy}^{(i)} + C_2\left[2\left(\sigma_{xx}^{(i)} + \sigma_{yy}^{(i)}\right)\sigma_{xy}^{(i)} + 2\sigma_{yz}^{(i)}\sigma_{xz}^{(i)}\right]\right\} dh. \tag{23}$$

Note that $C_1 = \alpha_1/\mu$ and $C_2 = \alpha_2/\mu^2$.

As described in Section 1, the second-order stress terms in Eqs. (22) and (23) have been neglected in recent photoelasticity studies, i.e., it has been assumed that $C_2 = 0$ [11, 13, 16, 37, 40]. This approach leads to the well-known equations of photoelasticity, as follows:

$$\Delta^{(i)} = C_1 dh\sigma_{d,sec}^{(i)} = C_1 dh\left|\sigma_{1,sec}^{(i)} - \sigma_{2,sec}^{(i)}\right| = C_1 dh\sqrt{\left(\sigma_{xx}^{(i)} - \sigma_{yy}^{(i)}\right)^2 + 4\left(\sigma_{xy}^{(i)}\right)^2}, \tag{24}$$

$$\phi^{(i)} = \frac{1}{2}\tan^{-1}\frac{2\sigma_{xy}^{(i)}}{\sigma_{xx}^{(i)} - \sigma_{yy}^{(i)}}, \tag{25}$$

where $\sigma_{d,sec}^{(i)}$ is the secondary principal stress difference and $\sigma_{1,sec}^{(i)}$ and $\sigma_{2,sec}^{(i)}$ are the maximum and minimum values of the secondary principal stress, respectively. Hereinafter, we refer to Eqs. (24) and (25) together as the "first-order stress-optic law", which is often simply called the "stress-optic law" in conventional photoelasticity studies. On the other hand, we call Eqs. (22) and (23) with $C_2 \neq 0$ the "second-order stress-optic law" in the the remainder of this paper.

Finally, we can calculate the retardation Δ using the first- and second-order stress-optic laws with integrated photoelasticity if the stress field is known a priori. In this study, we compare the calculated retardation with the experimentally measured retardation.

2.3. Measurement of the experimental retardation field

A schematic diagram of the experimental setup is shown in Fig. 2. A linear polarizer, a quarter-wave plate, and a square channel (made of quartz) are placed between a light source of 520-nm wavelength and a polarization camera (CRYSTA PI-5WP, Photron, temporal resolution: 1,000 f.p.s., spatial resolution: 732 × 280 pixels for an 8-bit light intensity image). Each pixel of the image sensor of the polarization camera consists of four linear polarizers with four different directions: 0°, 45°, 90°, and 135° [see Fig. 2(b)], which function as the analyzer in Eq. (8). The retardation of the polarized light is obtained from the light intensity values using software (Photron Ltd., CRYSTA Stress Viewer). The spatial resolution of the retardation data is 366 × 140 pixels, which is a quarter of 732 × 280 pixels. To reduce noise, measurement data are averaged over time and space. Since the measurement target is a steady laminar flow, the flow field is assumed to be constant in the flow direction and in time. Therefore, the measurement retardation is spatially averaged in the flow direction (x-direction) and averaged over a period of 1 s.

The flow inlet of the square channel is defined as $x = 0$ mm. The coordinate system is set up as shown in Fig. 2. The length of the square channel is 60 mm and the cross-section size is 2 mm × 2 mm. The fluid is supplied using a syringe pump to produce a steady laminar flow. The flow rates are 15, 20, 25, and 30 ml/min. The Reynolds number Re is 217 at the maximum flow rate of 30 ml/min. The measurement area is at $x = 45$ mm because the entrance length is 30 mm at the maximum flow rate (30 ml/min).

The working fluid is a CNC suspension (Cellulose Lab Ltd.). The CNC is mixed with ultrapure water using a magnetic stirrer (CHPS-170DF, ASONE Co., Ltd.) at 25 °C and 600 rpm for at least 1 hour. The CNC suspension is then sonicated using an ultrasonic processor (UX-300, Mitsui Electric Co. Ltd.) for 10 minutes. The ultrasonic processor also reduces the error between the experimental and theoretical orientation, as reported in a previous study [15, 16]. The concentration of the CNC suspension is set to 0.5 wt%. Figure 3 shows results for the shear viscosity η versus shear rate $\dot{\gamma}$ of the CNC suspension (0.5 wt%) and ultrapure water measured using a rheometer (MCR302, Anton Paar Co. Ltd.). The CNC suspension (0.5 wt%) can be regarded as a Newtonian fluid and its shear viscosity is 1.2 mPa·s.

2.4. Theoretical retardation field for a steady laminar flow in a square channel

In this section, we describe the calculation of the theoretical retardation field. First, the velocity distribution $u_x(y,z)$ of a steady laminar flow in a rectangular channel is derived from the following Navier–Stokes equations [41, 42].

$$\left(\frac{\partial^2}{\partial y^2} + \frac{\partial^2}{\partial z^2}\right) u_x = -\frac{4Q}{wb^3K}, \tag{26}$$

$$K = \frac{16}{3} - \frac{1024}{\pi^5}\frac{b}{w}\sum_{n=0}^{\infty}\frac{1}{(2n-1)^5}\tanh\frac{(2n-1)\,\pi w}{2h}, \tag{27}$$

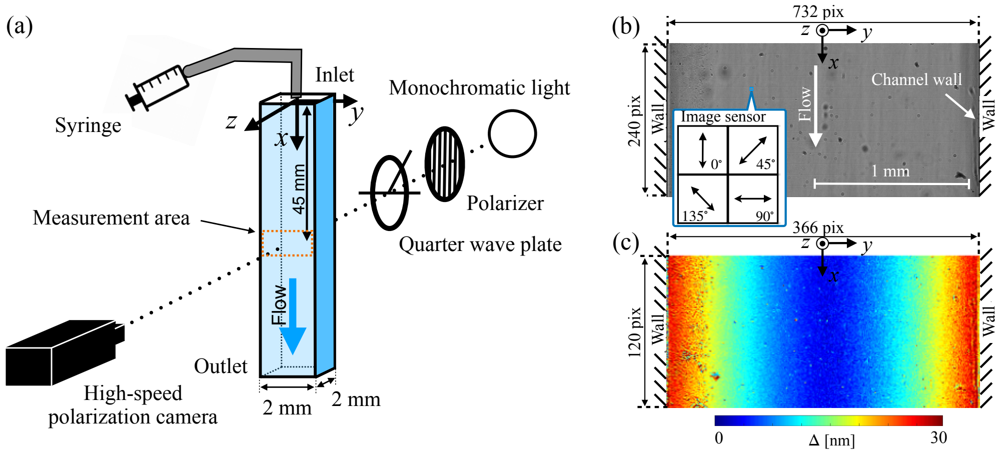

Fig. 2. (a) A schematic diagram of the experimental setup. (b) A raw image taken by the polarization camera. As shown in the inset, the neighboring pixels are polarizers with different directions. The retardation is measured from the intensity values of the four pixels. (c) The distribution of the measured retardation Δ. The spatial resolution of the retardation image is 1/4 of that of the light intensity image.

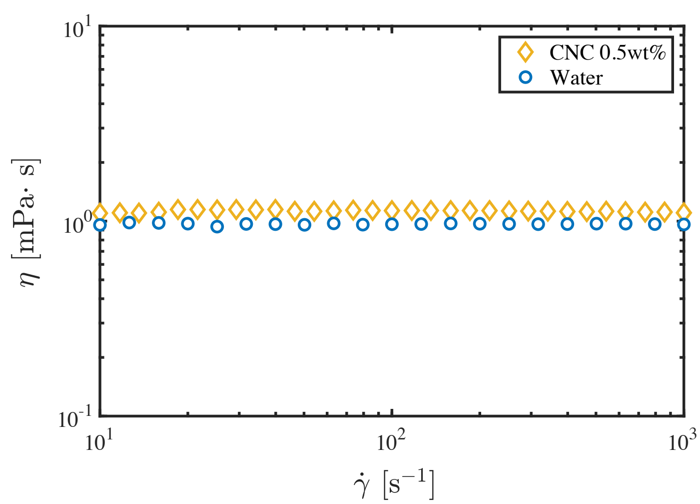

Fig. 3. The shear viscosity η versus the shear rate $\dot{\gamma}$ of the CNC suspension (0.5 wt%) and ultra-pure water measured using a rheometer.

where Q [m^3/s] is the flow rate, and w [m] and b [m] are the channel width and channel depth, respectively. The velocity distribution $u_x(y,z)$, which satisfies Eqs. (26) and (27), and the no-slip boundary condition at the wall ($y = \pm 1$ mm or $z = \pm 1$ mm) can be defined as follows:

$$u_x(y,z) = \frac{64Q}{wb\pi^3 K}\sum_{n=0}^{\infty}\frac{(-1)^n}{(2n+1)^3}\left[1 - \frac{\cosh\left(\frac{(2n+1)\pi y}{2b}\right)}{\cosh\left(\frac{(2n+1)\pi w}{2h}\right)}\right]\cos\left(\frac{(2n+1)\pi z}{2b}\right). \tag{28}$$

Note that the velocity $u_x(y, z)$ is proportional to the flow rate Q for a laminar flow. The theoretical velocity distribution in a square channel is shown in Fig. 4(a).

From Eq. (28), we calculate the velocity gradients, $\partial u_x/\partial y$ and $\partial u_x/\partial z$, as shown in Fig. 4(b,c). $\partial u_x/\partial y$ is zero at $y = 0$ and $z = \pm 1$ mm, while $\partial u_x/\partial z$ is zero at $z = 0$ and $y = \pm 1$ mm. The stress components used in the stress-optic laws can be calculated using these velocity gradients. For a steady laminar flow in a rectangular channel of a Newtonian fluid,

$$u_y = u_z = 0, \tag{29}$$

where u_y and u_z are the velocities in the y- and z- directions, respectively. Equations (28) and (29) yield

$$\dot{e}^{(i)}_{xx} = \dot{e}^{(i)}_{yy} = \dot{e}^{(i)}_{zz} = \dot{e}^{(i)}_{yz} = 0. \tag{30}$$

For a Newtonian fluid, the shear stress is proportional to the strain rate, i.e., $\sigma^{(i)}_{jk} = \mu\dot{e}^{(i)}_{jk}$, where μ is the liquid viscosity.

$$\sigma^{(i)}_{xx} = \sigma^{(i)}_{yy} = \sigma^{(i)}_{zz} = \sigma^{(i)}_{yz} = 0, \tag{31}$$

Figure 4 (d) and (e) shows the local distributions of the retardation, $\Delta^{(i)}_{\mathrm{1st}}$ and $\Delta^{(i)}_{\mathrm{2nd}}$, as calculated using the first-order stress-optic law [Eq. (24)] and the second-order stress-optic law [Eqs. (22) and (23)], respectively. At $y = 0$ mm and $z = \pm 1$ mm, there is a significant difference between the two retardation distributions — the value at $y = 0$, $z = \pm 1$ mm is zero for Δ_{1st} while it is non-zero for Δ_{2nd}. The theoretical retardation fields, Δ_{1st} and Δ_{2nd}, are finally obtained through integration along the camera's optical axis by integrating the local retardation using Mueller calculus [Eqs. (1)–(15)] with the first- and second-order stress-optic laws, respectively. Note that the theoretical retardation calculated through the aforementioned equations is proportional to the flow rate because the velocity is proportional to the flow rate.

3. Results and discussion

Figure 5(a) shows the measured retardation field at each flow rate. The retardation increases as the flow rate increases. The retardation is the highest at the channel wall ($y = \pm 1$ mm) and the lowest at the center of the channel ($y = 0$ mm) for all flow rates. The measured retardation averaged along the x-direction is plotted as the line profiles in Fig. 5(b). The retardation at each y-position increases with the flow rate. At $y = 1$ mm, the retardation values at flow rates of 15, 20, 25, and 30 ml/min are 16, 23, 29, and 34 nm, respectively. When the flow rate is 25 ml/min, which is about 83% of 30 ml/min, the retardation is about 86% of that at 30 ml/min. For flow rates of 20 ml/min (67%) and 15 ml/min (50%), the retardation values are about 68% and 48% of that at 30 ml/min, respectively. These results indicate a linear relationship between the retardation and the flow rate, as theoretically expected.

Figure 5(c) shows the normalized distributions of the experimental retardation and theoretical retardation as calculated using the first- and second-order stress-optic laws. The retardation is normalized so that the value at $y = 1$ mm is equal to 1. The normalized distributions of the experimental retardation are similar for all flow rates. The theoretical retardation calculated using the first-order stress optic law, Δ_{1st}, is shown as a gray solid line. As y approaches the center of the channel ($y = 0$ mm), the difference increases. The discrepancy at the center of the channel is consistent with measurement results reported in previous studies using similar setups [16, 27]. The stress component along the camera's optical axis (z-axis) is not considered in the first-order stress-optic law [Eq. (24)]. Therefore, the value of Δ_{1st} is zero at the center of the channel ($y = 0$ mm), where $\partial u_x/\partial y = 0$ [see Fig. 4(b)]. These results indicate that the first-order stress-optic law [Eq. (24)] is invalid around the center of the channel for a three-dimensional fluid flow. In contrast, the theoretical retardation calculated using the second-order stress-optic law (Δ_{2nd}, red solid line) is in good agreement with the experimental retardation for all flow rates, even

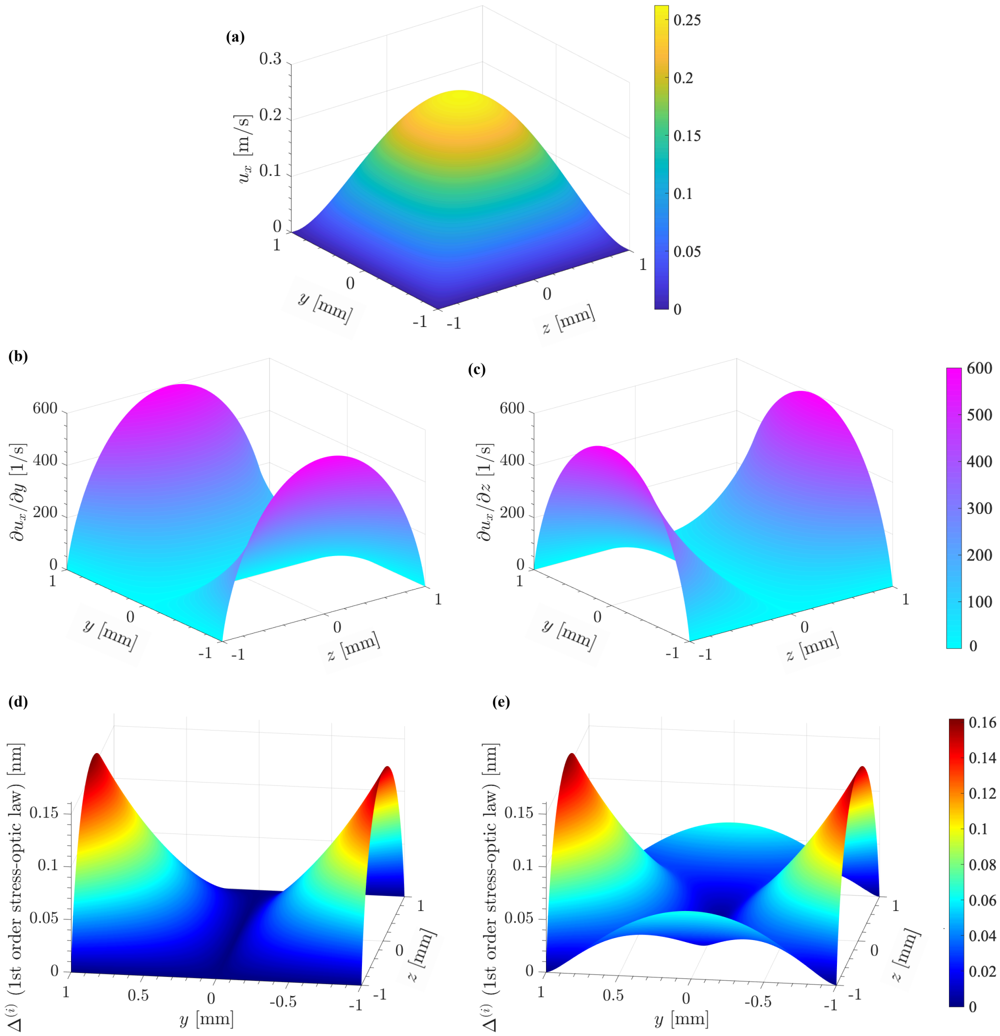

Fig. 4. (a) The velocity distribution $u(y,z)$ calculated from Eq. (28). (b) The velocity gradient distribution $\partial u_x/\partial y$. (c) The velocity gradient distribution $\partial u_x/\partial z$. (d) The local retardation $\Delta_{\text{1st}}^{(i)}$ calculated using the first-order stress-optic law [Eq. (24)]. (e) The local retardation $\Delta_{\text{2nd}}^{(i)}$ calculated using the second-order stress-optic law [Eqs. (22) and (23)]. The results here were calculated at a flow rate of 30 ml/min and under a stress-optic coefficient of $C_1 = 1.59 \times 10^{-5}$ 1/Pa. Note that (d) and (e) are integrated along the camera's optical axis (z-direction) using Eqs. (1)–(15), and are used to compare with the experimentally measured retardation.

around $y = 0$. The second-order term includes the stress component ($\sigma_{xz} = \mu\partial u_x/\partial z$) along the camera's optical axis. This is because at $y = 0$ mm, $\partial u_x/\partial y = 0$ while $\partial u_x/\partial z \neq 0$, so Δ_{2nd} has a non-zero value [see Fig. 4(c)]. Therefore, our result indicates that it is crucial to consider the second-order stress-optic law that includes the effect of the stress component along the camera's optical axis.

When the retardation is calculated using the second-order stress-optic law [Eqs. (22) and (23)],

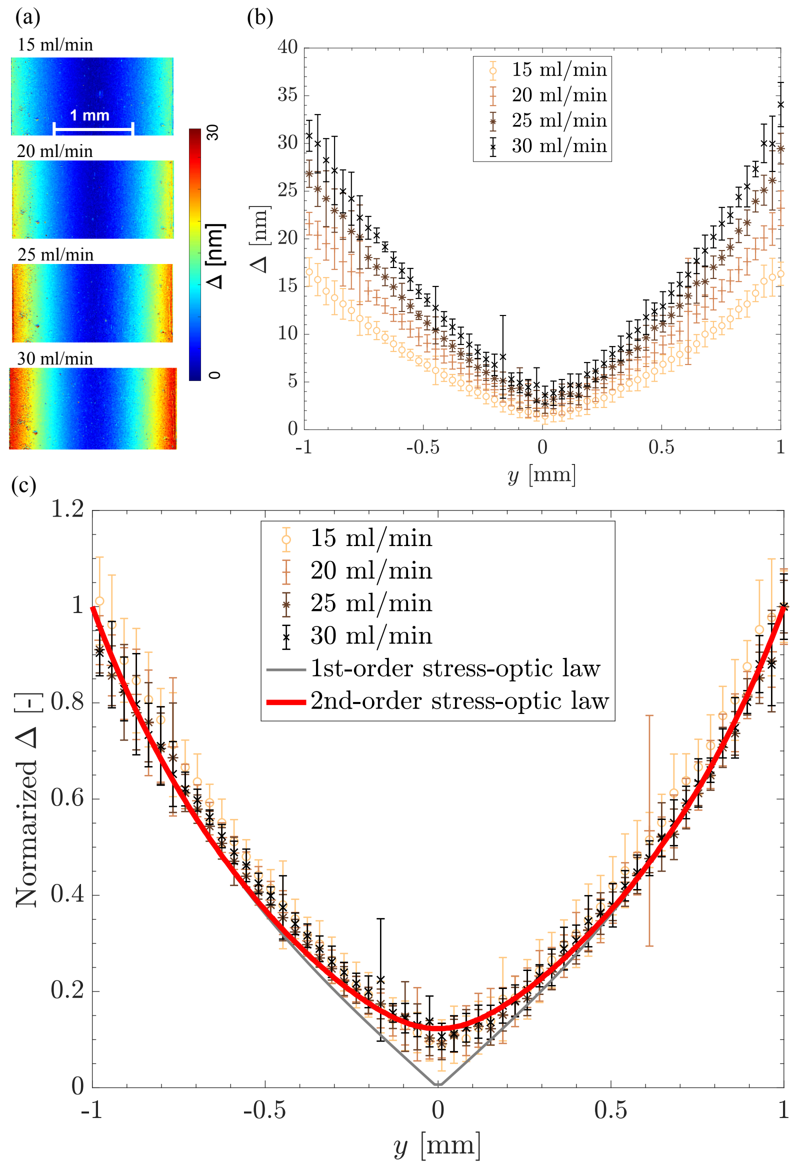

Fig. 5. (a) The measured retardation (Δ) distribution at flow rates of 15, 20, 25, and 30 ml/min. (b) The line profile of the retardation measurement results at flow rates of 15, 20, 25, and 30 ml/min. (c) A comparison between the spatial distribution of the experiment results and the spatial distribution of the theoretical retardation. The first-order stress-optic law is calculated by neglecting the second-order stress term in Eq. (24). The second-order stress-optic law includes the second-order stress term in Eqs. (22) and (23).

the values of the stress-optic coefficients, C_1 and C_2, must be found. However, the values of C_1 and C_2 for a CNC suspension (0.5 wt%) have not yet been reported to the author's knowledge. It is therefore necessary to define them now. We first determine the value of C_1. At the wall ($y = \pm 1$ mm), the shear rate ($\partial u_x / \partial z$) is equal to zero [Fig. 4(c)], i.e., σ_{xz} in Eqs. (22) and (23) equals zero. Thus, the C_2 term in the second-order stress-optic law becomes zero. Therefore, the value of C_1 can be determined by fitting the experimental and theoretical retardation at the wall. As a result, C_1 is estimated to be 1.61×10^{-5} Pa^{-1}. We next determine C_2 by considering the ratio of C_1 and C_2, which determines the normalized distribution of the second-order stress-optic law. As C_2 increases with respect to C_1, the value around the center of the channel increases. Therefore, we calculate the mean squared error between the experimental and theoretical retardation values when C_2/C_1 is varied between 0.1 and 2.0. It is found that the mean-square error has its minimum value when $C_2/C_1 \approx 1.1$. Therefore, $C_2 \approx 1.1C_1$, indicating that the contribution of the second-order term in the stress-optic law (i.e., stress components along the camera's optical axis) is of the same order as the first-order term.

4. Conclusion

In this study, we have validated the extended stress-optic law for a three-dimensional fluid flow using integrated photoelasticity. The focus was a steady laminar flow of Newtonian fluid (CNC 0.5 wt%) in a square channel, a case for which an analytical solution exists. The theoretical retardation was calculated using the concepts of integrated photoelasticity with a stress-optic law and an optically equivalent model. The experimental retardation was obtained by transmitting circularly-polarized light through the stress field and the corresponding retardation was measured using a high-speed polarization camera. It was found that when the second-order stress term in the stress-optic law [Eq. (22) and (23)] was neglected (first-order stress-optic law, $C_2 = 0$) as in previous studies (e.g., [13]), the normalized distributions of the theoretical and experimental retardation around the center of the channel disagreed with each other. In contrast, the theoretical retardation from the second-order stress-optic law showed good agreement ($C_2 \approx 1.1C_1$). We conclude that when a photoelastic measurement is applied to the three-dimensional flow of a CNC suspension, the second-order stress term in the stress-optic law, i.e., the stress component along the camera's optical axis, must be taken into account.

Acknowledgment

This work was supported by JSPS KAKENHI Grant Numbers JP20H00222, JP20H00223, JP20K14646, and JP22J13343, JST PRESTO Grant Number JPMJPR21O5, We thank Dr. T. Rösgen and Dr. C. Lane for their valuable discussions and suggestions, and Dr. T. Shikata for his advice on the preparation of the CNC suspension.

Data availability

Data underlying the results presented in this paper are not publicly available at this time but may be obtained from the authors upon reasonable request.

References

1. H. Aben, L. Ainola, and J. Anton, "Integrated photoelasticity for nondestructive residual stress measurement in glass," Opt. Lasers Eng. **33**, 49–64 (2000).
2. K. Ramesh and V. Ramakrishnan, "Digital photoelasticity of glass: A comprehensive review," Opt. Lasers Eng. **87**, 59–74 (2016).
3. N. K. Lautre, A. K. Sharma, P. Kumar, and S. Das, "A photoelasticity approach for characterization of defects in microwave drilling of soda lime glass," J. Mater. Process. Technol. **225**, 151–161 (2015).
4. J. Cernosek, "Three-dimensional photoelasticity by stress freezing," Exp. Mech. **20**, 417–426 (1980).
5. H. Aben and C. Guillemet, Photoelasticity of glass (Springer Science & Business Media, 2012).
6. R. Prabhakaran, "On the stress-optic law for orthotropic-model materials in biaxial-stress fields," Exp. Mech. **15**, 29–34 (1975).
7. H. Janeschitz-Kriegl, Polymer melt rheology and flow birefringence, vol. 6 (Springer Science & Business Media, 2012).
8. C. E. Knight Jr and H. Pih, "Orthotropic stress-optic law for plane stress photoelasticity of composite materials," Fibre Sci. Technol. **9**, 297–313 (1976).

9. J. F. Doyle and H. Danyluk, "Integrated photoelasticity for axisymmetric problems," Exp. Mech. **18**, 215–220 (1978).
10. R. C. Sampson, "A stress-optic law for photoelastic analysis of orthotropic composites," Exp. Mech. **10**, 210–215 (1970).
11. J. Riera and R. Mark, "The optical-rotation effect in photoelastic shell analysis," Exp. Mech. **9**, 9–16 (1969).
12. M. Walker, "Matrix calculus and the Stokes parameters of polarized radiation," Am. J. Phys. **22**, 170–174 (1954).
13. H. Aben and A. Puro, "Photoelastic tomography for three-dimensional flow birefringence studies," Inverse Probl. **13**, 215 (1997).
14. J. F. Doyle, "On a nonlinearity in flow birefringence," Exp. Mech. **22**, 37–38 (1982).
15. C. Lane, D. Rode, and T. Rösgen, "Birefringent properties of aqueous cellulose nanocrystal suspensions," Cellulose **29**, 1–15 (2022).
16. T. J. Ober, J. Soulages, and G. H. McKinley, "Spatially resolved quantitative rheo-optics of complex fluids in a microfluidic device," J. Rheol. **55**, 1127–1159 (2011).
17. M. Ito, Y. Yoshitake, and T. Takahashi, "Shear-induced structure change in shear-banding of a wormlike micellar solution in concentric cylinder flow," J. Rheol. **60**, 1019–1029 (2016).
18. V. Calabrese, S. Varchanis, S. J. Haward, and A. Q. Shen, "Alignment of colloidal rods in crowded environments," Macromolecules **55**, 5610–5620 (2022).
19. C. Lane, D. Rode, and T. Rösgen, "Optical characterization method for birefringent fluids using a polarization camera," Opt. Lasers Eng. **146**, 106724 (2021).
20. V. Calabrese, S. J. Haward, and A. Q. Shen, "Effects of shearing and extensional flows on the alignment of colloidal rods," Macromolecules **54**, 4176–4185 (2021).
21. V. Calabrese, S. Varchanis, S. J. Haward, J. Tsamopoulos, and A. Q. Shen, "Structure-property relationship of a soft colloidal glass in simple and mixed flows," J. Colloid Interface Sci. **601**, 454–466 (2021).
22. R. Kádár, S. Spirk, and T. Nypelo, "Cellulose nanocrystal liquid crystal phases: Progress and challenges in characterization using rheology coupled to optics, scattering, and spectroscopy," ACS nano **15**, 7931–7945 (2021).
23. C. Lane, "Shear rate imaging using a polarization camera and birefringent aqueous cellulose nanocrystal suspensions," Ph.D. thesis, ETH Zurich (2022).
24. D. Noto, Y. Tasaka, J. Hitomi, and Y. Murai, "Applicability evaluation of the stress-optic law in Newtonian fluids toward stress field measurements," Phys. Rev. Res. **2**, 043111 (2020).
25. W. J. McAfee and H. Pih, "Scattered-light flow-optic relations adaptable to three-dimensional flow birefringence," Exp. Mech. **14**, 385–391 (1974).
26. L. AINOLA, "Application of integrated photoelasticity to the determination of viscous flow velocity in closed conduits," Proc. Estonian Acad. Sci. Phys. Math. **47**, 48–55 (1998).
27. J. Kim, S. Michelin, M. Hilbers, L. Martinelli, E. Chaudan, G. Amselem, E. Fradet, J.-P. Boilot, A. M. Brouwer, C. N. Baroud et al., "Monitoring the orientation of rare-earth-doped nanorods for flow shear tomography," Nat. nanotechnology **12**, 914–919 (2017).
28. L. Srinath and A. Sarma, "Determination of the optically equivalent model in three-dimensional photoelasticity," Exp. Mech. **14**, 118–122 (1974).
29. L. Srinath, K. Ramesh, and V. Ramamurti, "Determination of characteristic parameters in three-dimensional photoelasticity," Opt. Eng. **27**, 225–230 (1988).
30. A. Pawlak and A. Galeski, "Determination of stresses around beads in stressed epoxy resin by photoelasticity," J. applied polymer science **86**, 1436–1444 (2002).
31. Y. Yokoyama, B. R. Mitchell, A. Nassiri, B. L. Kinsey, Y. P. Korkolis, and Y. Tagawa, "Integrated photoelasticity in a soft material: phase retardation, azimuthal angle, and stress-optic coefficient," Opt. Lasers Eng. **161**, 107335 (2023).
32. K. Ramesh and S. Sasikumar, "Digital photoelasticity: Recent developments and diverse applications," Opt. Lasers Eng. **135**, 106186 (2020).
33. T. Onuma and Y. Otani, "A development of two-dimensional birefringence distribution measurement system with a sampling rate of 1.3 mhz," Opt. communications **315**, 69–73 (2014).
34. Y. Otani, T. Shimada, T. Yoshizawa, and N. Umeda, "Two-dimensional birefringence measurement using the phase shifting technique," Opt. Eng. **33**, 1604–1609 (1994).
35. A. Asundi, "Phase shifting in photoelasticity," Exp. Tech. **17**, 19–23 (1993).
36. H. Aben and C. Guillemet, "Integrated photoelasticity," in Photoelasticity of Glass, (Springer, 1993), pp. 86–101.
37. L. Srinath and A. Sarma, "Effects of stress-induced optical activity in photoelasticity," J. Phys. D: Appl. Phys. **5**, 883 (1972).
38. G. G. Stokes, "On the composition and resolution of streams of polarized light from different sources," Trans. Camb. Philos. Soc. **9**, 399 (1851).
39. K. Ramesh, Developments in Photoelasticity (IOP Publishing, 2021).
40. B. Mitchell, Y. Yokoyama, A. Nassiri, Y. Tagawa, Y. P. Korkolis, and B. L. Kinsey, "An investigation of hertzian contact in soft materials using photoelastic tomography," J. Mech. Phys. Solids **171**, 105164 (2023).
41. F. Delplace, "Laminar flow of Newtonian liquids in ducts of rectangular cross-section a model for both physics and mathematics," Open Access J. Math. Theor. Phys. **1**, 198–201 (2018).
42. H. Nagamoto, Y. Kobayashi, J. Otomo, and E. Oshima, "Laminar flow characteristics in a rectangular microchannel," Kagaku Kougaku Ronbunshu **32**, 293–296 (2006).